Controllable $\mathcal{PT}$ phase transition and asymmetric soliton scattering in atomic gases with linear and nonlinear potentials

Lu Qin,[1] Chao Hang,[1,3,*] and Guoxiang Huang[1,2,3,†]

[1]*State Key Laboratory of Precision Spectroscopy, East China Normal University, Shanghai 200062, China*

[2]*Collaborative Innovation Center of Extreme Optics, Shanxi University, Taiyuan, Shanxi 030006, China*

[3]*NYU-ECNU Institute of Physics, New York University at Shanghai, Shanghai 200062, China*

(Received 2 January 2019; published 24 April 2019)

We propose a physical scheme to realize combined linear and nonlinear optical potentials with parity-time ($\mathcal{PT}$) symmetry and investigate the scattering property of optical solitons in a coherent atomic gas. We show that the combined linear and nonlinear $\mathcal{PT}$-symmetric potentials can be created through the spatial modulation of the control laser field and the inclusion of the Kerr nonlinearity of the signal laser field. We demonstrate that the imaginary part of the nonlinear $\mathcal{PT}$ potential plays a crucial role for the occurrence of the $\mathcal{PT}$ phase transition and the change of the $\mathcal{PT}$ phase diagram, which can be actively manipulated in our system. We demonstrate also that the system supports stable optical solitons, which can be managed via tuning the combined linear and nonlinear $\mathcal{PT}$ potentials; furthermore, by taking the combined linear and nonlinear $\mathcal{PT}$ potentials as a defect, the scattering of the optical solitons by the defect displays evident asymmetric behavior, controlled by the imaginary parts of the combined linear and nonlinear $\mathcal{PT}$ potentials. The results reported here may have potential applications in optical information processing and transmission.

DOI: 10.1103/PhysRevA.99.043832

I. INTRODUCTION

In recent years, considerable attention has focused on the research of parity-time ($\mathcal{PT}$) symmetry in various physical systems. The primary motivation for such research is to develop non-Hermitian quantum theory [1,2]. Because of the mathematical equivalence of the Maxwell equation in electrodynamics under paraxial approximation with the Schrödinger equation in quantum mechanics, light propagations in electromagnetic media provide excellent platforms for testing $\mathcal{PT}$-symmetric quantum theory both theoretically and experimentally [3]. With the advance of research, it has been found that $\mathcal{PT}$-symmetric optics, or more generally non-Hermitian photonics [4,5], may have many practical applications, including the realization of unidirectional light propagations [6–10], coherent perfect absorbers [11–13], giant light amplification [14], novel lasers [15,16], precision measurement [17,18], quantum computation [19], and so on. Optical solitons [20], and more generally nonlinear waves, in $\mathcal{PT}$-symmetric systems have also been explored [21].

Recently, it has been shown that coherently atomic gases interacting with laser fields may provide a fertile ground for studying optical $\mathcal{PT}$ symmetry [22–26]. The optical refractive index of such systems can be actively manipulated; furthermore, the Kerr nonlinearity in such systems can be greatly increased by using the resonant enhancement of nonlinear optical susceptibilities. Thus, the non-Hermitian optics with coherent atomic gases opens a new route for the investigation of $\mathcal{PT}$-symmetric linear and nonlinear quantum mechanics. It was predicted that weak-light solitons are possible in $\mathcal{PT}$-symmetric atomic gases [27,28].

However, most optical $\mathcal{PT}$ symmetries realized so far are only for linear systems, or for nonlinear ones with constant Kerr coefficients. Because in many cases space-dependent Kerr coefficients occur or are needed, it is desirable to obtain $\mathcal{PT}$-symmetric systems that not only have a linear potential but also have a nonlinear one with a space-dependent Kerr coefficient [21]. In this paper, we propose a realistic scheme for physically realizing combined linear and nonlinear optical potentials with $\mathcal{PT}$ symmetry by using a coherent atomic gas, through a spatial modulation of the control laser field and the inclusion of the Kerr nonlinearity of the signal laser field. We shall show that the space-dependent imaginary part of the nonlinear $\mathcal{PT}$ potential plays a key role for the occurrence of the $\mathcal{PT}$ phase transition and the change of the $\mathcal{PT}$ phase diagram, which can be actively manipulated. We shall also show that the system supports stable optical solitons, which can be managed via tuning the combined $\mathcal{PT}$ potentials; furthermore, by taking such combined $\mathcal{PT}$ potentials as a defect, the scattering of the optical solitons by the defect displays obvious asymmetric behavior, controlled mainly by the space-dependent imaginary parts of the combined linear and nonlinear potentials.

Before proceeding, we notice that in literature there were many studies devoted to $\mathcal{PT}$-symmetric systems with a space-dependent nonlinear potential, or with space-dependent combined linear and nonlinear ones [29–36]. Results on the soliton scattering in systems with $\mathcal{PT}$ symmetry were also reported [37–41]. However, in many aspects our paper is different from Refs. [29–41]. First, in Refs. [29–41] no realistic physical scheme on how to realize space-dependent $\mathcal{PT}$

*chang@phy.ecnu.edu.cn

†gxhuang@phy.ecnu.edu.cn

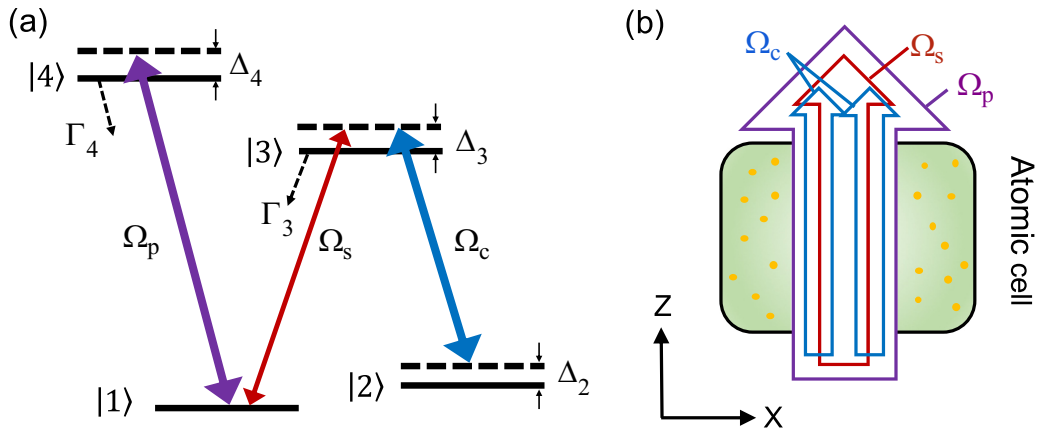

FIG. 1. (a) Energy-level diagram and excitation scheme of the N-type four-level atomic gas. $|j\rangle$ are atomic states and Δ_j are detunings ($j = 1, 2, 3, 4$; $\Delta_1 = 0$); Γ_3 and Γ_4 are, respectively, decay rates of $|3\rangle$ and $|4\rangle$; Ω_s, Ω_c, and Ω_p are, respectively, half Rabi frequencies of three laser fields, i.e., weak signal field (red), strong control field (blue), and strong pump field (purple). The pump field provides an active Raman gain to the signal field. (b) Atomic cell (yellow solid circles denote atoms) and the geometric arrangement of the three laser fields. Especially, the control field consists of two spatially separated Gaussian beams used to realize the combined linear and nonlinear $\mathcal{PT}$ optical potentials. All laser fields are assumed to propagate through the atomic ensemble along the z direction.

potentials was provided. Our paper presents a practical scheme for realizing the combined linear and nonlinear $\mathcal{PT}$ potentials, which is useful to guide realistic experiments. Second, in Refs. [29–41], no result on the manipulation of $\mathcal{PT}$ phase transition by tuning the space-dependent nonlinear $\mathcal{PT}$ potential was given. In our paper, such manipulation is studied and the result reveals that the property of the $\mathcal{PT}$ phase transition has a heavy dependence on the space-dependent imaginary part of the nonlinear $\mathcal{PT}$ potential. Third, in Refs. [29–41] no scattering of the soliton was considered for systems that have a nonlinear $\mathcal{PT}$ potential with a space-dependent imaginary part. In our paper, such scattering is investigated in detail and interesting results (especially on the asymmetric and nonreciprocal soliton scattering) are obtained. The results reported here are useful for developing non-Hermitian nonlinear optics and have potential applications in optical information processing and transmission.

The paper is arranged as follows. In Sec. II, a description of the physical model under study is presented. In Secs. III, the realization of the combined linear and nonlinear $\mathcal{PT}$ potentials by engineering the space-dependent control field is provided. In Sec. IV, the results on the controlled $\mathcal{PT}$ phase transition and stable optical solitons are studied. In Sec. V, the scatterings of optical solitons by the $\mathcal{PT}$-symmetric linear and nonlinear optical potentials are analyzed. Finally, Sec. VI summaries the main results obtained in this paper.

II. MODEL

We start with considering a cold, dilute N-type four-level atomic gas, which interacts with a weak signal laser field $\mathbf{E}_s$ of center frequency ω_s and wave number $k_s = \omega_s/c$, a strong control laser field $\mathbf{E}_c$ of frequency ω_c and wave number $k_c = \omega_c/c$, and a strong pump-laser field $\mathbf{E}_p$ of frequency ω_p and wave number $k_p = \omega_p/c$, coupling to transitions $|1\rangle \leftrightarrow |3\rangle$, $|2\rangle \leftrightarrow |3\rangle$, and $|1\rangle \leftrightarrow |4\rangle$, respectively [see Fig. 1(a)]. The electric-field vector can be written as $\mathbf{E} = \mathbf{E}_s + \mathbf{E}_c + \mathbf{E}_p = \sum_{l=s,c,p} \mathbf{e}_l \mathcal{E}_l \exp[i(k_l z - \omega_l t)] + \text{c.c.}$, where $\mathbf{e}_s$, $\mathbf{e}_c$, and $\mathbf{e}_p$ ($\mathcal{E}_s$, $\mathcal{E}_c$, and $\mathcal{E}_p$) are, respectively, polarization unit vectors (envelopes) of the signal, control, and pump fields. For minimizing Doppler effect, all laser fields are assumed to propagate through the atomic ensemble along the z direction. The atomic excitation scheme given by Fig. 1(a) can be taken as a system of optically pumped electromagnetically induced transparency (EIT), consisting of a standard three-level Λ-type EIT plus an optical pumping used to provide an active Raman gain to the signal field [42].

Under electric-dipole and rotating-wave approximations and in the interaction picture, the Hamiltonian of this optically pumped EIT system is given by $\hat{H}_{\text{int}} = -\hbar \sum_{j=1}^{4} \Delta_j |j\rangle\langle j| - \hbar[\Omega_p|4\rangle\langle 1| + \Omega_s|3\rangle\langle 1| + \Omega_c|3\rangle\langle 2| + \text{H.c.}]$. Here $\Delta_2 = \omega_s - \omega_c - (E_2 - E_1)/\hbar$ is two-photon detuning, $\Delta_3 = \omega_c - (E_3 - E_1)/\hbar$ and $\Delta_4 = \omega_p - (E_4 - E_1)/\hbar$ are one-photon detunings (with E_j the eigenenergy of the atomic state $|j\rangle$), and $\Omega_s = (\mathbf{e}_s \cdot \mathbf{p}_{13})\mathcal{E}_s/\hbar$, $\Omega_c = (\mathbf{e}_c \cdot \mathbf{p}_{23})\mathcal{E}_c/\hbar$, and $\Omega_p = (\mathbf{e}_p \cdot \mathbf{p}_{14})\mathcal{E}_p/\hbar$ are, respectively, half Rabi frequencies of the signal, control, and pump fields, with $\mathbf{p}_{jl}$ the electric dipole matrix elements associated with the transition $|j\rangle \leftrightarrow |l\rangle$.

The dynamics of atoms is governed by the optical Bloch equation

$$\frac{\partial \rho}{\partial t} = -\frac{i}{\hbar}[\hat{H}_{\text{int}}, \rho] - \Gamma[\rho], \tag{1}$$

where ρ is a 4×4 density matrix (with density-matrix elements ρ_{jl}; $j, l = 1, 2, 3, 4$) describing the atomic population and coherence, and Γ is a 4×4 relaxation matrix describing the spontaneous emission and dephasing. The explicit expression of Eq. (1) is presented in Appendix A.

The motion of the signal field is described by the Maxwell equation, which under the slowly varying envelope approximation reads [25]

$$i\left(\frac{\partial}{\partial z} + \frac{1}{c}\frac{\partial}{\partial t}\right)\Omega_s + \frac{c}{2\omega_s}\left(\frac{\partial^2}{\partial x^2} + \frac{\partial^2}{\partial y^2}\right)\Omega_s + \frac{\omega_s}{2c}\chi_s\Omega_s = 0, \tag{2}$$

where $\chi_s = \mathcal{N}_a|\mathbf{e}_s \cdot \mathbf{p}_{13}|^2\rho_{31}/(\varepsilon_0\hbar\Omega_s)$ is the optical susceptibility of the signal field, with $\mathcal{N}_a$ the atomic density and ε_0 the vacuum dielectric constant. We are interested in the stationary state of the system, i.e., the time derivatives in the Maxwell-Bloch Eqs. (1) and (2) can be neglected, which is valid for the signal field with a longer time duration.

Since the signal field is weak, we can take Ω_s as a small parameter to solve the Bloch Eq. (1) by using a perturbation expansion. The solution of Eq. (1) up to third order is presented in Appendix B. With this solution we may obtain the expression of the total optical susceptibility of the signal field with the form $\chi_s = \chi_s^{(1)} + |\Omega_s|^2\chi_s^{(3)}$, where $\chi_s^{(1)} = \mathcal{N}_a|\mathbf{e}_s \cdot \mathbf{p}_{13}|^2 a_{31}^{(1)}/(\varepsilon_0\hbar)$ and $\chi_s^{(3)} = \mathcal{N}_a|\mathbf{e}_s \cdot \mathbf{p}_{13}|^2 a_{31}^{(3)}/(\varepsilon_0\hbar)$ are, respectively, first-order and third-order nonlinear optical susceptibilities, with explicit expressions of $a_{31}^{(1)}$ and $a_{31}^{(3)}$, respectively, given by Eqs. (B2b) and (B5) in Appendix B. For simplicity, we assume that the signal, control, and pump fields have a wide distribution in the y direction, so that their y dependence plays no significant role during the propagation of the signal field, and hence the term $\partial^2\Omega_s/\partial y^2$ in Eq. (2) can be disregarded.

To get space-dependent linear and nonlinear optical potentials, we assume that the control field is modulated along the x direction, i.e., $\Omega_c = \Omega_c(x)$. Then one has $\chi_s^{(1)} = \chi_s^{(1)}(x)$, $\chi_s^{(3)} = \chi_s^{(3)}(x)$, and Eq. (2) is reduced to

$$i\frac{\partial\Omega_s}{\partial z} + \frac{1}{2k_s}\frac{\partial^2\Omega_s}{\partial x^2} + \frac{k_s}{2}\chi_s^{(1)}(x)\Omega_s + \frac{k_s}{2}\chi_s^{(3)}(x)|\Omega_s|^2\Omega_s = 0. \tag{3}$$

For the convenience of the following calculations, we convert Eq. (3) into the dimensionless form

$$i\frac{\partial u}{\partial\zeta} = -\frac{\partial^2 u}{\partial\xi^2} + V(\xi)u + W(\xi)|u|^2u, \tag{4}$$

where we have defined dimensionless variables $\xi = x/l_s$, $\zeta = z/(2k_sl_s^2)$, and $u = \Omega_s/U_0$, with U_0 and l_s, respectively, the typical half Rabi frequency and typical length in the x direction (comparable to the wavelength $\lambda_s = 2\pi c/\omega_s$) of the signal field. In Eq. (4), $V(\xi) = -k_s^2l_s^2\chi_s^{(1)}(\xi)$ and $W(\xi) = -k_s^2l_s^2|U_0|^2\chi_s^{(3)}(\xi)$, which, following Ref. [21], are called, respectively, linear and nonlinear potentials, or combined linear and nonlinear potentials.

III. PHYSICAL REALIZATION OF THE COMBINED LINEAR AND NONLINEAR $\mathcal{PT}$-SYMMETRIC POTENTIALS

Although there were many studies on $\mathcal{PT}$-symmetric systems with combined linear and nonlinear potentials [29–36], no realistic scheme was provided for their physical realization up to now. Here we show that it is possible to realize such potentials through choosing suitable system parameters and a space-dependent control field in the optically pumped EIT system described above.

Before presenting the concrete form of the spatially modulated Ω_c for realizing the combined linear and nonlinear optical potentials obeying $\mathcal{PT}$ symmetry, we illustrate the relation between the linear and nonlinear optical susceptibilities of the signal field and the control-field frequency detuning Δ_2 for a fixed $\Omega_c = \Omega_{c0}$. We take $\Delta_3 = \Delta_4 = 0$, $\Gamma_{12} = \Gamma_{34} \approx 0$, $\Gamma_{13} = \Gamma_{23} = \Gamma_{14} = \Gamma_{24} = 6\pi$ MHz, $\Omega_s = 0.1 \times 2\pi$ MHz, $\Omega_p = 4 \times 2\pi$ MHz, $\Omega_{c0} = 1.5 \times 2\pi$ MHz, and solve Eq. (1) numerically, with the results of $\chi_s^{(1)}$ and $\chi_s^{(3)}$ plotted in Figs. 2(a) and 2(d), respectively. The blue solid and red dashed lines in Fig. 2(a) [Fig. 2(d)] are, respectively, the real part $\mathrm{Re}[\chi_s^{(1)}]$ and imaginary part $\mathrm{Im}[\chi_s^{(1)}]$ of the linear susceptibility (real part $\mathrm{Re}[\chi_s^{(3)}]$ and imaginary part $\mathrm{Im}[\chi_s^{(3)}]$ of the nonlinear susceptibility). We see that $\mathrm{Im}[\chi_s^{(1)}]$ and $\mathrm{Im}[\chi_s^{(3)}]$ are simultaneously zero for $\Delta_2 = -29.94$ MHz, i.e., point "P" in Figs. 2(a) and 2(d). In the vicinity of this "P" point, $\chi_s^{(1)}$ exhibits absorption on the left side and gain on the right side; in contrast, $\chi_s^{(3)}$ exhibits gain in the left side and absorption in the right side of the "P" point.

A symmetric real part and an antisymmetric imaginary part of $\chi_s^{(1)}$ and $\chi_s^{(3)}$ can be acquired by choosing different Δ_2. Shown in Figs. 2(b) and 2(e) are $\mathrm{Re}[\chi_s^{(1)}]$ and $\mathrm{Re}[\chi_s^{(3)}]$ as functions of $\Omega_{c0}/(2\pi)$. The blue solid lines and red dashed lines are for $\Delta_2 = -28.68$ and -31.98 MHz, respectively. We see that $\mathrm{Re}[\chi_s^{(j)}]|_{\Delta_2=-28.68\,\mathrm{MHz}} \approx \mathrm{Re}[\chi_s^{(j)}]|_{\Delta_2=-31.98\,\mathrm{MHz}}$ $(j = 1, 3)$, which means that both the real parts of the linear and nonlinear susceptibilities are matched well, i.e., they are symmetric. Figures 2(c) and 2(f) show results of $\mathrm{Im}[\chi_s^{(1)}]$ and $\mathrm{Im}[\chi_s^{(3)}]$ as functions of $\Omega_{c0}/(2\pi)$. One finds that $\mathrm{Im}[\chi_s^{(j)}]|_{\Delta_2=-28.68\,\mathrm{MHz}} \approx -\mathrm{Im}[\chi_s^{(j)}]|_{\Delta_2=-31.98\,\mathrm{MHz}}$ $(j = 1, 3)$, i.e., the imaginary parts of the linear and nonlinear susceptibilities are antisymmetric [43].

The above fact tells us that the $\mathcal{PT}$ symmetry of the combined linear and nonlinear potentials $V(\xi)$ and $W(\xi)$ can be realized by choosing a control field that consists of two spatially separated laser beams with different frequency detunings, which produce two separated waveguides where one provides absorption and other one provides gain for the propagation of the signal field. With this thought in mind, to fulfill the condition of $\mathcal{PT}$ symmetry, i.e., $V^*(-\xi) = V(\xi)$ and $W^*(-\xi) = W(\xi)$, equivalent to $\mathrm{Re}[\chi_s^{(j)}(x)] = \mathrm{Re}[\chi_s^{(j)}(-x)]$ and $\mathrm{Im}[\chi_s^{(j)}(x)] = -\mathrm{Im}[\chi_s^{(j)}(-x)]$ $(j = 1, 3)$, we naturally assume that the control field consists of two identical (but spatially separated) Gaussian beams with the form

$$\Omega_c(x) = \Omega_{c0}\left[e^{-\frac{(x-x_0)^2}{2\sigma^2}} + e^{\frac{-(x+x_0)^2}{2\sigma^2}}\right], \tag{5}$$

where $2x_0$ is the separation between the two beams, and σ is the width of each beam [44]. Though these two beams have identical intensity profiles, one can obtain gain in one beam and absorption in another for both the linear and nonlinear susceptibilities by choosing different frequency detunings for each beam, as discussed above. Substituting Eq. (5) into the expressions of $\chi_s^{(j)}(x)$ $(j = 1, 3)$, we obtain the following $\mathcal{PT}$-symmetric, dimensionless combined linear and nonlinear potentials:

$$V(\xi) = V_0 + v_0\left[\left(e^{\frac{-(\xi-d)^2}{2a^2}} + e^{\frac{-(\xi+d)^2}{2a^2}}\right) + iv_1\left(e^{\frac{-(\xi-d)^2}{2a^2}} - e^{\frac{-(\xi+d)^2}{2a^2}}\right)\right], \tag{6a}$$

$$W(\xi) = W_0 + w_0\left[\left(e^{\frac{-(\xi-d)^2}{2a^2}} + e^{\frac{-(\xi+d)^2}{2a^2}}\right) - iw_1\left(e^{\frac{-(\xi-d)^2}{2a^2}} - e^{\frac{-(\xi+d)^2}{2a^2}}\right)\right], \tag{6b}$$

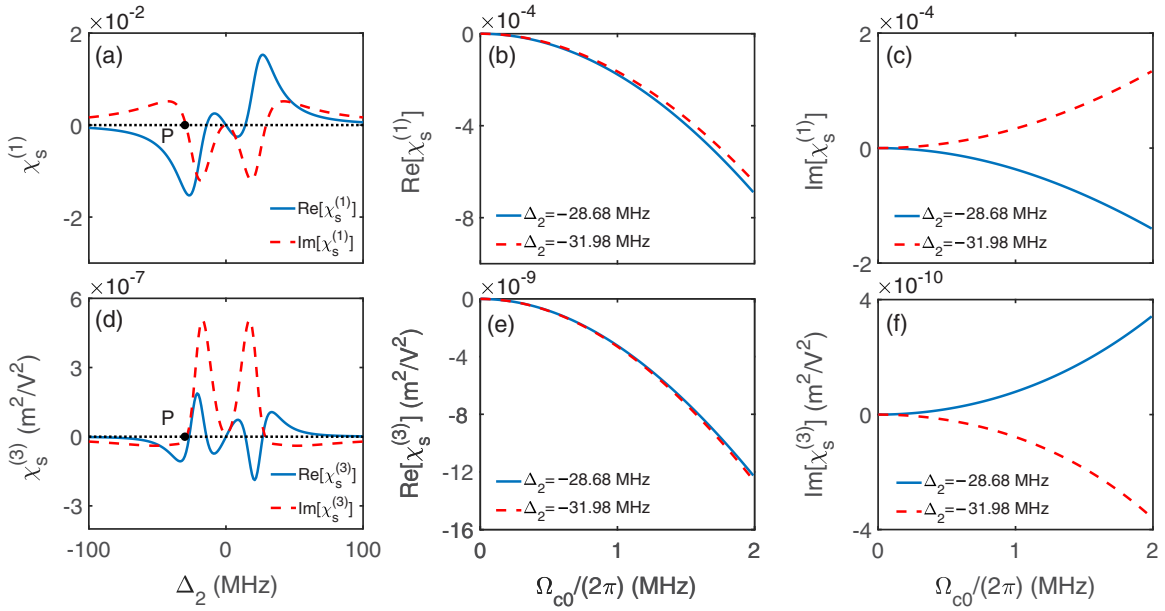

FIG. 2. Realization of the linear and nonlinear optical susceptibilities with $\mathcal{PT}$ symmetry. (a) Real part Re[$\chi_s^{(1)}$] (blue solid line) and imaginary part Im[$\chi_s^{(1)}$] (red dashed line) of the linear susceptibility $\chi_s^{(1)}$ as functions of Δ_2. (d) Similar to (a) but for the nonlinear susceptibility $\chi_s^{(3)}$. Point "P" in (a) and (d) corresponds to $\Delta_2 = -29.94$ MHz. (b) Real part Re[$\chi_s^{(1)}$] as a function of $\Omega_{c0}/(2\pi)$ for $\Delta_2 = -28.68$ (blue solid line) and $\Delta_2 = -31.98$ MHz (red dashed line), respectively. (e) Similar to (b) but for the real part of the nonlinear susceptibility, i.e., Re[$\chi_s^{(3)}$]. (c) Imaginary part Im[$\chi_s^{(1)}$] via $\Omega_{c0}/(2\pi)$ for $\Delta_2 = -28.68$ (blue solid line) and $\Delta_2 = -31.98$ MHz (red dashed line), respectively. (f) Similar to (c) but for the imaginary part of the nonlinear susceptibility, i.e., Im[$\chi_s^{(3)}$].

where V_0 and W_0 are constants, v_0 (w_0) is the amplitude of the space-dependent part for the linear potential V (nonlinear potential W), and v_1 ($-w_1$) is the relative amplitude between the imaginary part and the real part of V (W), with $d = x_0/l_s$ and $a = \sigma/l_s$.

Spatial profiles of $V(\xi)$ and $W(\xi)$ are shown in Figs. 3(a) and 3(b), respectively. When plotting the figure, system parameters are chosen to be $v_0 = 2$, $w_0 = 0.8$, $v_1 = 0.25$, $w_1 = 0.06$, $d = 10$, and $a = 4.2$, corresponding to $\Omega_{c0} = 2\pi \times 10^6$ s^{-1}, $x_0 = 10\,\mu$m, and $\sigma = 4\,\mu$m in Eq. (5). From Eq. (6) and Fig. 3 we see that, as expected, both the linear potential $V(\xi)$ and the nonlinear potential $W(\xi)$ exhibit indeed $\mathcal{PT}$ symmetry. With the specific form of the control field (5), both Re(V) and Re(W) have double-well shapes (blue solid lines); for the linear potential there is an absorption on the left side [Im(V) < 0] and a gain on the right side [Im(V) > 0], but for the nonlinear potential there is a gain on the left side [Im(W) > 0] and an absorption on the right side [Im(W) < 0], illustrated by the red dash-dotted lines in the figure. Notice that the method for realizing the $\mathcal{PT}$-symmetric potentials described here is a generation of that developed in Ref. [23]; however, it is different from Ref. [23] since it is valid for preparing both the linear and nonlinear $\mathcal{PT}$-symmetric potentials simultaneously.

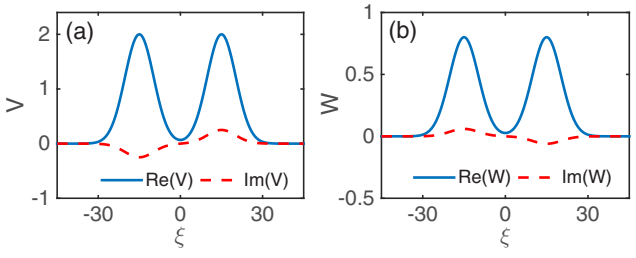

FIG. 3. Spatial profiles of the linear $\mathcal{PT}$ potential V and nonlinear $\mathcal{PT}$ potential W as functions of ξ. (a) Profile of the linear $\mathcal{PT}$ potential $V(\xi)$. The blue solid line and red dash-dotted line are its real part Re(V) and imaginary part Im(V), respectively. (b) The same as (a) but for the nonlinear $\mathcal{PT}$ potential $W(\xi)$. Constants V_0 and W_0 in Eq. (6) have been disregarded when plotting the figure.

IV. CONTROLLABLE $\mathcal{PT}$ PHASE TRANSITION AND STABLE SOLITON PROPAGATION

A. $\mathcal{PT}$ phase transitions and their active control

We now turn to consider the property of the $\mathcal{PT}$ phase transition of our optically pumped EIT system with the combined linear and nonlinear $\mathcal{PT}$ potentials (6). Because the system can be actively controlled, the $\mathcal{PT}$ phase transition may be manipulated by tuning system parameters, e.g., potential parameters v_1 and w_1 in Eq. (6).

To demonstrate this, we assume $u(\zeta, \xi) = u_0(\xi)e^{iq\zeta}$, and from Eq. (4) we obtain the nonlinear eigenvalue problem $\partial^2 u_0/\partial\xi^2 - V(\xi)u_0 - W(\xi)|u_0|^2 u_0 = qu_0$, where q is the eigenvalue (also called the propagation constant) and $u_0(\xi)$ is the eigenfunction. This eigenvalue problem can be solved numerically by using the Newton iteration method [45]. One of the key characters of $\mathcal{PT}$ symmetry is that the eigenvalue displays a transition from real to complex when the relative amplitudes of the linear and nonlinear potentials, i.e., v_1 and w_1, are varied. Shown in Fig. 4(a) is the result obtained for the phase diagram of the $\mathcal{PT}$ phase transition in the plane

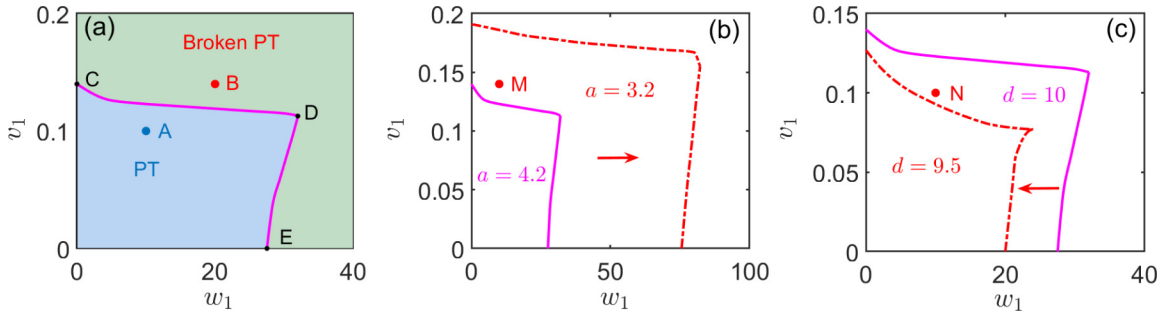

FIG. 4. $\mathcal{PT}$ phase diagrams and their active manipulation. (a) $\mathcal{PT}$ phase diagram of the system as functions of v_1 and w_1 with $a = 4.2$ and $d = 10$. The left-bottom (blue) domain is the phase with $\mathcal{PT}$ symmetry, while the top-right (green) domain is the phase with broken $\mathcal{PT}$ symmetry. The purple solid line is the boundary between the unbroken and broken $\mathcal{PT}$ phases, where points "C," "D," and "E" correspond to $(w_1, v_1) = (0, 0.14)$, (32,0.11), and (28, 0), respectively. Point "A" (point "B") corresponds to $(w_1, v_1) = (10, 0.1)$ [$(w_1, v_1) = (20, 0.15)$], where the optical soliton is stable (unstable). (b) $\mathcal{PT}$ phase diagram with $a = 3.2$ (the boundary of the $\mathcal{PT}$ phase transition is denoted by the red dash-dotted line) and $a = 4.2$ (the boundary of the $\mathcal{PT}$ phase transition is denoted by the purple solid line). Point "M" corresponds to $(v_1, w_1) = (10, 0.14)$. (c) $\mathcal{PT}$ phase diagram with $d = 9.5$ (the boundary of the $\mathcal{PT}$ phase transition is denoted by the red dash-dotted line) and $d = 10$ (the boundary of the $\mathcal{PT}$ phase transition is denoted by the purple solid line). Point "N" corresponds to $(v_1, w_1) = (10, 0.1)$. The red arrow indicates the changing trend of the boundary of the $\mathcal{PT}$ phase transition.

of v_1 and w_1 for $a = 4.2$ and $d = 10$, with other system parameters the same as used in Fig. 3. The purple solid line in the figure represents the boundary of the $\mathcal{PT}$ phase transition, with the left-bottom (blue) domain being the phase with $\mathcal{PT}$ symmetry and the top-right (green) domain being the phase with broken $\mathcal{PT}$ symmetry. Points "C," "D," and "E" in the boundary line correspond to $(w_1, v_1) = (0, 0.14)$, (32,0.11), and (28, 0), respectively. From Fig. 4(a), we see that the $\mathcal{PT}$ phase transition depends not only on v_1 but also on w_1. To be specific, for a linear $\mathcal{PT}$-symmetric potential, i.e., $v_1 > 0$, and a real nonlinear potential, i.e., $w_1 = 0$, the phase transition point locates at $v_1 = 0.14$ (labeled by "C"). However, this value will be decreased when w_1 increases. Therefore, the imaginary part of the nonlinear potential can enlarge the broken domain of $\mathcal{PT}$ symmetry. Furthermore, the $\mathcal{PT}$ phase transition is determined by the ratio between the imaginary and real parts of the combined linear and nonlinear potentials, which is determined by the quantity $(v_0 v_1 - w_0 w_1 |u|^2)/(v_0 + w_0 |u|^2)$, with $|u|^2$ the intensity of the signal field. Since this ratio decreases as $|u|^2$ increases, the broken domain of $\mathcal{PT}$ symmetry can be enlarged by increasing the signal field intensity.

Except for v_1 and w_1, the $\mathcal{PT}$ phase diagram can also be changed by adjusting the width (characterized by the parameter a) of each beam in the control field. Shown in Fig. 4(b) are phase boundary lines of the $\mathcal{PT}$ phase transition for different values of a [with other system parameters the same as those used in Fig. 4(a)], where the purple solid and red dash-dotted lines are for $a = 4.2$ and 3.2, respectively. From the figure, we see that the domain of the $\mathcal{PT}$-symmetry phase is increased greatly as a is decreased. The red arrow in the figure represents the changing trend of the boundary of the $\mathcal{PT}$ phase transition.

The threshold of the $\mathcal{PT}$-symmetry breaking depends also on the separation (characterized by the parameter d) of the two beams in the control field. Figure 4(c) shows the $\mathcal{PT}$ phase diagram by decreasing d from 10 to 9.5, with other system parameters the same as those used in Fig. 4(a). In the figure, the purple solid and red dash-dotted lines represent the boundary lines of the $\mathcal{PT}$ phase transition for $d = 10$ and 9.5, respectively. One sees that the domain of the $\mathcal{PT}$-symmetry phase is decreased when d decreases.

Based on the results given by panels (a), (b), and (c) of Fig. 4, we conclude that the $\mathcal{PT}$ phase transition in our optically pumped EIT system can indeed be manipulated by adjusting the parameters w_1, v_1, a, and d in the combined linear and nonlinear potentials (6), which provide a practical physical example for an active control of non-Hermitian nonlinear optical systems.

B. Stable soliton propagations and their active control

One of the important applications of the controllability of the $\mathcal{PT}$ phase transition is the soliton propagation in the combined linear and nonlinear $\mathcal{PT}$-symmetric potentials and their active control in the system. By solving Eq. (4) numerically, we find that the system supports optical solitons, with their intensity arrested in the spatial region between the two Gaussian peaks of the control field; furthermore, such optical solitons are stable when the system works in the domain of the $\mathcal{PT}$ symmetry, and they become unstable if the system works in the domain of the broken $\mathcal{PT}$ symmetry.

Shown in Fig. 5(a) is the numerical result on the propagation of a fundamental optical soliton, with $(w_1, v_1) = (10, 0.1)$ to make the system work in the $\mathcal{PT}$-symmetric phase, i.e., point "A" in Fig. 4(a). We see that the optical soliton is fairly stable during propagation. Figure 5(b) shows the propagation of another optical soliton, with $(w_1, v_1) = (20, 0.15)$ to make the system work in the broken $\mathcal{PT}$-symmetric phase, i.e., point "B" in Fig. 4(a). In this case, the soliton propagation is unstable. For a better understanding on the results shown in Figs. 5(a) and 5(b), a linear stability analysis [46,47] on the soliton is carried out (see Appendix C), which shows that the optical soliton described in Fig. 5(a) [Fig. 5(b)] is indeed stable (unstable).

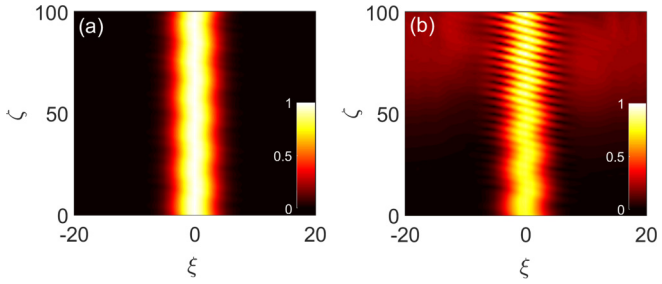

FIG. 5. Optical solitons in the system. (a) Stable propagation of an optical soliton, with $(w_1, v_1) = (10, 0.1)$ where the system works in the $\mathcal{PT}$-symmetric phase, i.e., point "A" in Fig. 4(a). (b) Unstable propagation of an optical soliton, with $(w_1, v_1) = (20, 0.15)$ where the system works in the broken $\mathcal{PT}$-symmetric phase, i.e., point "B" in Fig. 4(a).

The active control of the optical soliton can be implemented by adjusting the width a of the two Gaussian peaks in the combined linear and nonlinear potentials (6). To show this, we focus on the case $(w_1,\ v_1)$=(10, 0.14), i.e., point "M" in Fig. 4(b). In this case, the system works in the $\mathcal{PT}$-symmetry phase for $a = 3.2$ but the broken $\mathcal{PT}$-symmetry phase for $a = 4.2$. Shown in Fig. 6(a) is the result on the propagation of an optical soliton by tuning the value of a. The upper part of the figure is the variation of a along the ζ axis; the lower part is the propagation behavior of the soliton in different regions of ζ. We see that the soliton is stable in the region $0 < \zeta < 50$ (where $a = 3.2$), while it is not stable in the region $50 < \zeta < 100$ (where $a = 4.2$).

Similarly, the active control of the optical soliton can also be realized by tuning the separation d between the two Gaussian peaks in the linear and nonlinear $\mathcal{PT}$-symmetric potentials (6). To illustrate this, we consider the case $(w_1,\ v_1)$=(10, 0.1), i.e., point "N" in Fig. 4(c). In this situation, the system works in the $\mathcal{PT}$-symmetry phase for $d = 10$ but the broken $\mathcal{PT}$-symmetry phase for $d = 9.5$. Plotted in Fig. 6(b) is the result on the propagation of the optical soliton by tuning the

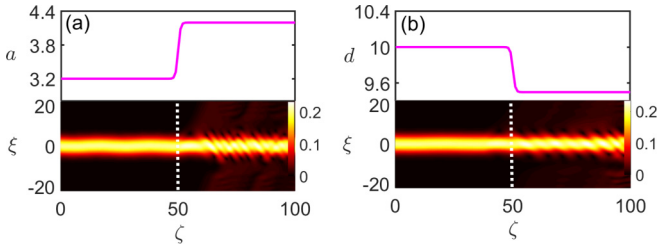

FIG. 6. Active control of optical solitons. (a) Optical soliton for $(w_1, v_1) = (10, 0.14)$ [corresponding to the "M" point in Fig. 4(b)]. Upper part: The variation of the width a of the two Gaussian peaks in the combined linear and nonlinear $\mathcal{PT}$-symmetric potentials along the ζ axis. Lower part: Propagation behaviors of the soliton in the regions $0 < \zeta < 50$ ($a = 3.2$) and $50 < \zeta < 100$ ($a = 4.2$). (b) Optical soliton for $(w_1, v_1) = (10, 0.1)$ [corresponding to the "N" point in Fig. 4(c)]. Upper part: The variation of the separation d between the two Gaussian peaks in the combined linear and nonlinear $\mathcal{PT}$-symmetric potentials along the ζ axis. Lower part: Propagation behaviors of the soliton in the regions $0 < \zeta < 50$ ($d = 10$) and $50 < \zeta < 100$ ($d = 9.5$).

value of d. The upper part is the variation of d along the ζ axis; the lower part shows the propagation behaviors of the soliton for different ζ. One sees that the soliton is stable in the region $0 < \zeta < 50$ (where $d = 10$), while it is not stable in the region $50 < \zeta < 100$ (where $d = 9.5$).

As we see, the results presented in Figs. 5 and 6 are quite consistent with the predictions given in Fig. 4, which means that optical soliton propagations and their stability can indeed be controlled by changing the $\mathcal{PT}$ potential parameters w_1, v_1, a, and d.

V. ASYMMETRIC SOLITON SCATTERING BY THE COMBINED LINEAR AND NONLINEAR OPTICAL POTENTIALS

A. Symmetric soliton scattering

The scattering property of solitons is an interesting research topic not only for a deep understanding of the physical property but also for possible practical applications of nonlinear $\mathcal{PT}$-symmetric systems. It is natural to ask the question of how the soliton scattering works in our optically pumped EIT system if the combined $\mathcal{PT}$-symmetric optical potentials are taken to be a defect. Parameters of the defect are chosen to be $v_0 = 2$, $w_0 = 0.8$, $a = 4.2$, and $d = 10$. To this end, we assume that the position of the soliton is initially away from the defect, so that there is no interaction between them at $\zeta = 0$. In general, we may have full reflection, transmission, trapping, or some combination of them. These scattering behaviors can be described by the coefficients of reflection (R), transmission (T), and trapping (G), defined, respectively, by

$$R = \frac{1}{P}\int_{-\infty}^{-h} |\psi(\xi)|^2 d\xi, \quad T = \frac{1}{P}\int_{h}^{\infty} |\psi(\xi)|^2 d\xi,$$
$$G = \frac{1}{P}\int_{-h}^{h} |\psi(\xi)|^2 d\xi, \tag{7}$$

where $P = \int_{-\infty}^{\infty} |\psi(\xi)|^2 d\xi$ is the total power of the optical soliton and h denotes position on the ξ axis at which the influence of the defect on the soliton is negligible.

We first consider the situation with $(w_1, v_1) = (0, 0)$ in Eq. (6), i.e., the scattering of the soliton by a defect with real linear and nonlinear potentials. Shown in Fig. 7(a) [Fig. 7(b)] is the result of the soliton scattering when the soliton is incident from the left side of the defect with incident velocity $v = 0.8$ ($v = 1.5$). The result is obtained through numerically solving Eq. (4) by using the split-step Fourier method [45] and taking $u(\xi, \zeta = 0) = 1.5\mathrm{sech}(\xi)\, e^{iv\xi}$ [48]. In the figure, the region between the two vertical white dashed lines denotes the one where the defect locates; the width of the defect is $\Delta\xi = 40$ in the ξ direction and $\Delta\zeta = \infty$ in the ζ direction. We see that, for smaller (larger) incident velocity, the soliton is completely reflected (transmitted). Figure 7(c) illustrates the result of the reflection coefficient R (red solid line) and transmission coefficient T (green dash-dotted line) as functions of incident velocity v. The blue dots "a" and "b" in the figure indicate the values of R and T, which correspond to the cases shown in panels (a) and (b), respectively. We find that when $v \geqslant v_{\mathrm{cr}}$ (where $v_{\mathrm{cr}} \approx 1$ is critical velocity) the scattering

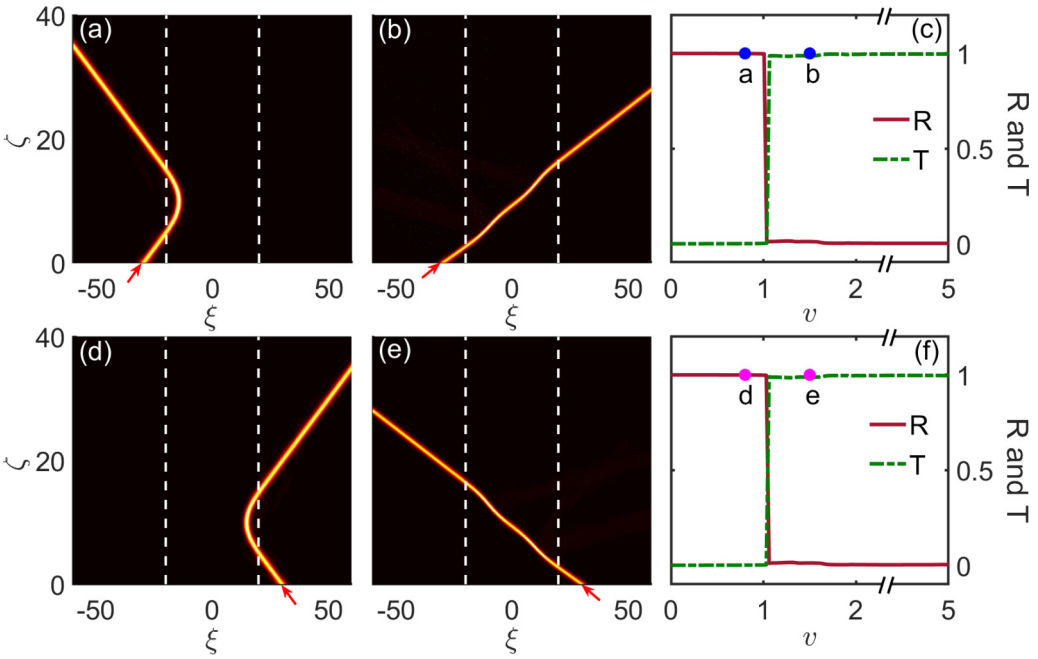

FIG. 7. Symmetric soliton scattering by the combined but real linear and nonlinear $\mathcal{PT}$-symmetric defect potentials, i.e., $(w_1, v_1) = (0, 0)$ in Eq. (6). In panels (a), (b), (d), and (e), the region between the two vertical white dashed lines is the one where the defect locates. (a) [(b)] The soliton is incident from the left side of the defect with incident velocity $v = 0.8$ ($v = 1.5$). (c) Reflection coefficient R (red solid line) and transmission coefficient T (green dash-dotted line) as functions of incident velocity v for the soliton incident from the left side. The blue dots "a" and "b" represent the values of R and T for the cases shown in panels (a) and (b), respectively. (d) [(e)] The soliton is incident from the right side with incident velocity $v = 0.8$ ($v = 1.5$). (f) Reflection coefficient R (red solid line) and transmission coefficient T (green dash-dotted line) as functions of incident velocity v for the soliton incident from the right side. The purple dots "d" and "e" represent the values of R and T for the cases shown in panels (d) and (e), respectively.

of the soliton changes sharply from a full reflection to a full transmission. There is nearly no trapping of the soliton, i.e., $G = 0$, during the process of the soliton scattering.

For comparison, in Fig. 7(d) [Fig. 7(e)] we show the result of the soliton scattering when the soliton is incident from the right side of the defect with incident velocity $v = 0.8$ ($v = 1.5$). One sees that for small ($v = 0.8$) and large ($v = 1.5$) incident velocity the soliton is also completely reflected (transmitted). Figure 7(f) plots the reflection coefficient R (red solid line) and transmission coefficient T (green dash-dotted line) as functions of incident velocity v. The red dots "d" and "e" indicate the values of R and T for the cases shown in panels (d) and (e), respectively. It is found that when $v \geqslant v_{\rm cr} \approx 1$ the scattering of the soliton changes also from a full reflection to a full transmission sharply. Similar to the case of the scattering from the left side, there is nearly no trapping during the process of the soliton scattering. From these results, we conclude that, for the combined real linear and nonlinear $\mathcal{PT}$ defect potentials, the soliton scattering is left-right symmetric (reciprocal).

B. Asymmetric soliton scattering

We now consider what will happen for the soliton scattering if the imaginary parts of the combined linear and nonlinear $\mathcal{PT}$ potentials are not zero, by taking $(w_1, v_1) = (0, 0.1)$ in Eq. (6) and other parameter values the same as those used in Fig. 7. Panels (a), (b), and (c) of Fig. 8 show results of soliton scattering when the soliton is incident from the left side of the defect with $v = 0.4$, 1, and 3.5, respectively. We see that the soliton gets a complete reflection when it collides with the defect for a small incidence velocity [$v = 0.4$, panel (a)], and a complete transmission for a large incidence velocity [$v = 3.5$, panel (c)]. However, for an intermediate incidence velocity, the soliton experiences a state with a combination of reflection and transmission [$v = 1$, panel (b)], in which a radiation is generated and the reflected wave undergoes an attenuation, which is due to the absorption on the left side of the defect [see Fig. 3(a)]. Plotted in Fig. 8(d) are reflection coefficient R (red solid line), trapping coefficient G (blue dashed line), and transmission coefficient T (green dash-dotted line) as functions of v. Blue dots indicate the value of R and T corresponding to panels (a), (b), and (c), respectively. We see that there exists an interval of the incident velocity, i.e., $0.9 < v < 1.2$, in which the trapping coefficient G is nonzero. Thus, by tuning v one can control the ratio between the reflected and transmitted parts of the soliton, which might be useful to design an optical soliton beam splitter.

Shown in panels (e), (f), and (g) of Fig. 8 are results of the soliton scattering when the soliton is incident from the right side of the defect with the incident velocity $v = 0.4$, 1, and 3.5, respectively. One sees that for small and large incident velocity [panels (e) and (g)] the soliton scattering displays similar behaviors to those shown in panels (a) and (c), but there exists an interval, i.e., $0.42 < v < 2.8$, in which the soliton undergoes a *collapse* when it collides with the defect [see Fig. 8(f)]. Figure 8(h) gives the reflection coefficient R (red solid line) and transmission coefficient T (green dash-dotted

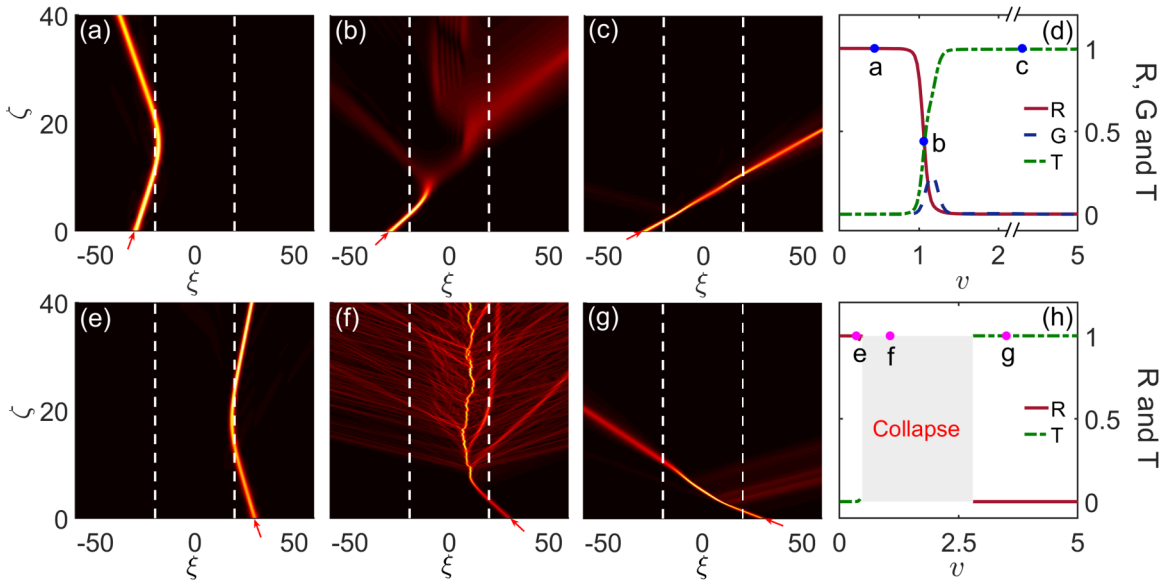

FIG. 8. Asymmetric soliton scattering by the combined linear and nonlinear $\mathcal{PT}$-symmetric defect with $(w_1, v_1) = (0, 0.1)$. Panels (a), (b), and (c) are the soliton scatterings by the defect when the soliton is incident from the left side with the incidence velocity $v = 0.4$, 1, and 3.5, respectively. (d) Reflection coefficient R (red solid line), trapping coefficient G (blue dashed line), and transmission coefficient T (green dash-dotted line) as functions of v. Blue dots indicate the value of R and T corresponding to panels (a), (b), and (c), respectively. Panels (e), (f), and (g) are the soliton scatterings by the defect when the soliton is incident from the right side with the incidence velocity $v = 0.4$, 1, and 3.5, respectively. (h) Reflection coefficient R (red solid line) and transmission coefficient T (green dash-dotted line) as functions of v. The gray domain is the one where the soliton is collapsed. Purple dots indicate the values of R and T corresponding to panels (e), (f), and (g), respectively.

line) as functions of v. The gray domain is the one where the soliton is collapsed. Purple dots indicate the values of R and T corresponding to panels (e), (f), and (g), respectively. Comparing the upper panels with the lower panels of Fig. 8, one sees that the left-right symmetry and reciprocity of the soliton scattering are broken.

Lastly, we investigate the soliton scattering by a defect if the imaginary parts of the combined linear and nonlinear $\mathcal{PT}$ potentials are not nonzero, by taking $(w_1, v_1) = (0.1, 0.1)$, and other system parameters are the same as used in Fig. 7. Shown in panels (a), (b), and (c) of Fig. 9 are results of the soliton scattering when the soliton is incident from the left side, with the incident velocity $v = 0.2$, 4.2, and 4.5, respectively. Figure 9(d) gives the reflection coefficient R (red solid line) and transmission coefficient T (green dash-dotted line) as functions of v. Purple dots indicate the values of R and T corresponding to panels (a), (b), and (c), respectively. Panels (e), (f), and (g) illustrate results of the soliton scattering when the soliton is incident from the right side with $v = 0.2$, 4.2, and 4.5, respectively. Figure 9(h) gives the reflection coefficient R (red solid line) and transmission coefficient T (green dash-dotted line) as functions of v. Purple dots indicate the values of R and T corresponding to panels (e), (f), and (g), respectively.

From Fig. 9, we see that for small and large incident velocities the soliton scatterings have similar behaviors for the both left and right incidences. However, in the domain of the intermediate incident velocity the soliton scatterings have quite different behaviors. Figure 9(b) [Fig. 9(f)] shows the soliton scattering for $v = 4.2$, where the soliton is completely transmitted (trapped). In fact, no complete self-trapping is found for the soliton when it collides the defect from the left side, but there exists an interval of v, i.e., $0.26 < v < 4.25$, in which the soliton can experience a complete self-trapping when colliding with the defect from the right side. Based on these results, we conclude that the left-right symmetry and reciprocity of the soliton scattering are also broken when the imaginary parts of both the linear and nonlinear potentials are not zero.

VI. SUMMARY

In this paper, we have proposed a realistic physical scheme for realizing combined linear and nonlinear optical potentials with $\mathcal{PT}$ symmetry and investigated the interesting scattering properties of optical solitons in an optically pumped EIT system. We have shown that the combined linear and nonlinear $\mathcal{PT}$-symmetric potentials can be produced through the design of the spatial modulation of the control laser field and the inclusion of the Kerr nonlinearity of the signal laser field. We have demonstrated that the imaginary part of the nonlinear $\mathcal{PT}$ potential plays a very important role for the occurrence of the $\mathcal{PT}$ phase transition and the change of the $\mathcal{PT}$ phase diagram, which can be actively manipulated in our system. We have also demonstrated that the system supports stable optical solitons, which can be controlled via tuning the combined $\mathcal{PT}$ potentials. Furthermore, by taking the combined $\mathcal{PT}$ potentials as a defect the scattering of the optical solitons by the defect may display obvious asymmetric and nonreciprocal behaviors, which can be manipulated by the imaginary parts of the combined linear and nonlinear $\mathcal{PT}$ potentials. The results reported here may have potential applications in optical information processing and transmission.

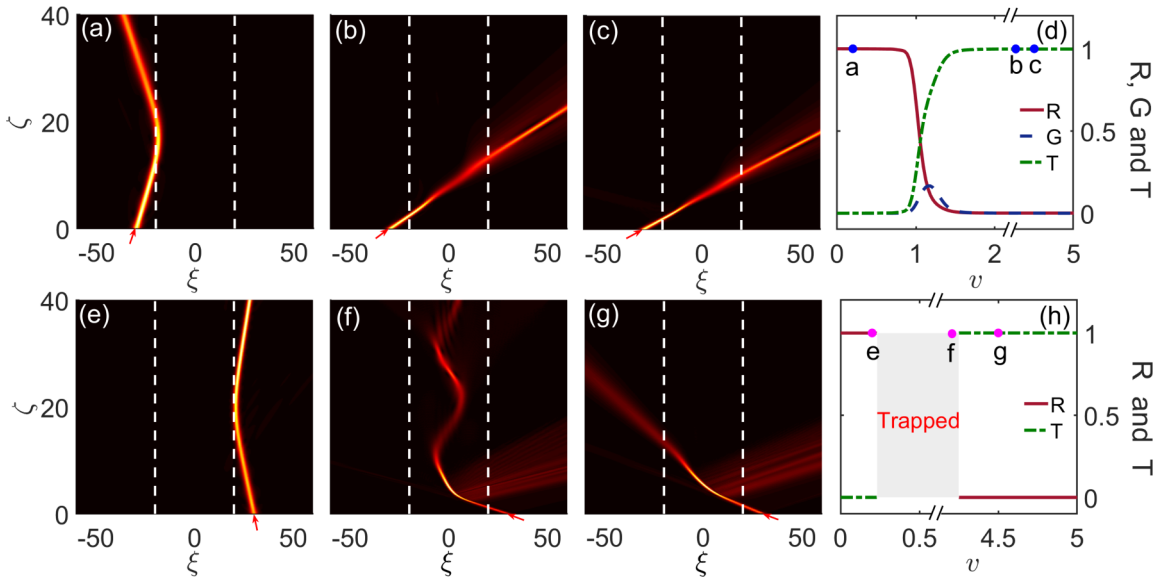

FIG. 9. Asymmetric soliton scattering by the combined linear and nonlinear $\mathcal{PT}$-symmetric defect with $(w_1, v_1) = (0.1, 0.1)$. Panels (a), (b), and (c) are the soliton scatterings when the soliton is incident from the left with the incidence velocity $v = 0.2$, 4.2, and 4.5, respectively. (d) Reflection coefficient R (red solid line), trapping coefficient G (blue dashed line), and transmission coefficient T (green dash-dotted line) as functions of v. Blue dots indicate the value of R and T corresponding to panels (a), (b) and (c), respectively. Panels (e), (f), and (g) are the soliton scatterings when the soliton is incident from the right side with the incidence velocity $v = 0.2$, 4.2, and 4.5, respectively. (h) Reflection coefficient R (red solid line) and transmission coefficient T (green dash-dotted line) as functions of v. The gray domain is the one where the soliton is trapped. Red dots indicate the values of R and T corresponding to panels (e), (f), and (g), respectively.

ACKNOWLEDGMENTS

This work was supported by National Natural Science Foundation of China under Grants No. 11475063 and No. 11474099 and by National Key Research and Development Program of China under Grant Nos. 2016YFA0302103 and 2017YFA0304201.

APPENDIX A: OPTICAL BLOCH EQUATION

The optical Bloch equation describing the time evolution of the density-matrix elements ρ_{jl} reads [49]

$$i\frac{\partial}{\partial t}\rho_{22} - i\Gamma_{42}\rho_{44} - i\Gamma_{32}\rho_{33} + \Omega_c^*\rho_{32} - \Omega_c\rho_{32}^* = 0, \tag{A1a}$$

$$i\frac{\partial}{\partial t}\rho_{33} + i\Gamma_3\rho_{33} + \Omega_s\rho_{31}^* - \Omega_s^*\rho_{31} + \Omega_c\rho_{32}^* - \Omega_c^*\rho_{32} = 0, \tag{A1b}$$

$$i\frac{\partial}{\partial t}\rho_{44} + i\Gamma_4\rho_{44} + \Omega_p\rho_{41}^* - \Omega_p^*\rho_{41} = 0, \tag{A1c}$$

$$\left(i\frac{\partial}{\partial t} + d_{21}\right)\rho_{21} + \Omega_c^*\rho_{31} - \Omega_s\rho_{32}^* - \Omega_p\rho_{42}^* = 0, \tag{A1d}$$

$$\left(i\frac{\partial}{\partial t} + d_{31}\right)\rho_{31} + \Omega_s(\rho_{11} - \rho_{33}) + \Omega_c\rho_{21} - \Omega_p\rho_{43}^* = 0, \tag{A1e}$$

$$\left(i\frac{\partial}{\partial t} + d_{41}\right)\rho_{41} + \Omega_p(\rho_{11} - \rho_{44}) - \Omega_s\rho_{43} = 0, \tag{A1f}$$

$$\left(i\frac{\partial}{\partial t} + d_{32}\right)\rho_{32} + \Omega_c(\rho_{22} - \rho_{33}) + \Omega_s\rho_{21}^* = 0, \tag{A1g}$$

$$\left(i\frac{\partial}{\partial t} + d_{42}\right)\rho_{42} - \Omega_c\rho_{43} + \Omega_p\rho_{21}^* = 0, \tag{A1h}$$

$$\left(i\frac{\partial}{\partial t} + d_{43}\right)\rho_{43} + \Omega_p\rho_{31}^* - \Omega_s^*\rho_{41} - \Omega_c^*\rho_{42} = 0, \tag{A1i}$$

where the symbol "*" denotes the complex conjugate, $d_{21} = \Delta_2 + i\gamma_{21}$, $d_{31} = \Delta_3 + i\gamma_{31}$, $d_{41} = \Delta_4 + i\gamma_{41}$, $d_{32} = \Delta_3 - \Delta_2 + i\gamma_{32}$, $d_{42} = \Delta_4 - \Delta_2 + i\gamma_{42}$, $d_{43} = \Delta_4 - \Delta_3 + i\gamma_{43}$, $\gamma_{jl} = (\Gamma_j + \Gamma_l)/2 + \gamma_{jl}^{\text{dep}}$ $(j \neq l)$, and $\Gamma_l = \sum_{j<l}\Gamma_{jl}$, with Γ_{jl} the

spontaneous emission decay rate and $\gamma_{jl}^{\rm dep}$ the dephasing rate from $|l\rangle$ to $|j\rangle$. The atomic population in the ground state ρ_{11} can be obtained by using the condition $\sum_{j=1}^{4}\rho_{jj}=1$ [49].

APPENDIX B: SOLUTIONS OF THE BLOCH EQUATION

By taking $\Omega_s\sim\epsilon$ as an expansion parameter, assuming the expansion $\rho_{jl}=\rho_{jl}^{(0)}+\epsilon\rho_{jl}^{(1)}+\epsilon^2\rho_{jl}^{(2)}+\cdots$, and substituting the expansion into the Bloch Eq. (1), we obtain a chain of linear but inhomogeneous equations, which can be solved order by order.

The zeroth-order solution reads

$$\rho_{11}^{(0)}=\frac{\Gamma_{31}X_{32}|\Omega_c|^2(i\Gamma_4+X_{41}|\Omega_p|^2)}{D}, \tag{B1a}$$

$$\rho_{22}^{(0)}=\frac{\Gamma_{42}X_{41}|\Omega_p|^2(i\Gamma_3+X_{32}|\Omega_c|^2)}{D}, \tag{B1b}$$

$$\rho_{33}^{(0)}=\frac{\Gamma_{42}X_{41}X_{32}|\Omega_p|^2|\Omega_c|^2}{D}, \tag{B1c}$$

$$\rho_{44}^{(0)}=\frac{\Gamma_{13}X_{41}X_{32}|\Omega_p|^2|\Omega_c|^2}{D}, \tag{B1d}$$

$$\rho_{32}^{(0)}=-\frac{i\Gamma_3\Gamma_{24}X_{41}|\Omega_p|^2\Omega_c}{d_{32}D}, \tag{B1e}$$

$$\rho_{41}^{(0)}=-\frac{i\Gamma_{13}\Gamma_4X_{32}|\Omega_c|^2\Omega_p}{d_{41}D}, \tag{B1f}$$

where $D=2(\Gamma_{31}+\Gamma_{42})X_{32}X_{41}|\Omega_p|^2|\Omega_c|^2+i\Gamma_4\Gamma_{31}X_{32}|\Omega_c|^2+i\Gamma_3\Gamma_{42}X_{41}|\Omega_p|^2$, with $X_{41}=1/d_{41}^*-1/d_{41}$, and $X_{32}=1/d_{32}^*-1/d_{32}$. Other $\rho_{jl}^{(0)}$ are zero. The first-order solution is given by

$$\begin{aligned}\rho_{21}^{(1)}=&\frac{(d_{31}d_{42}^*d_{43}^*+|\Omega_p|^2d_{42}^*-|\Omega_c|^2d_{31})\rho_{32}^{*(0)}-\Omega_c^*\big(\rho_{33}^{(0)}-\rho_{11}^{(0)}\big)(d_{42}^*d_{43}^*+|\Omega_p|^2-|\Omega_c|^2)}{a_1d_{31}+a_2|\Omega_p|^2-a_3|\Omega_c|^2}\Omega_s\\&+\frac{\Omega_p\Omega_c^*\rho_{41}^{(0)}(d_{31}-d_{42}^*)}{a_1d_{31}+a_2|\Omega_p|^2-a_3|\Omega_c|^2}\Omega_s\equiv a_{21}^{(1)}\Omega_s,\end{aligned} \tag{B2a}$$

$$\rho_{31}^{(1)}=\frac{a_1\big(\rho_{33}^{(0)}-\rho_{11}^{(0)}\big)+a_2\Omega_p\rho_{41}^{*(0)}-a_3\Omega_c\rho_{32}^{*(0)}}{a_1d_{31}+a_2|\Omega_p|^2-a_3|\Omega_c|^2}\Omega_s\equiv a_{31}^{(1)}\Omega_s, \tag{B2b}$$

$$\begin{aligned}\rho_{42}^{(1)}=&\frac{\Omega_c\Omega_p(d_{43}-d_{21}^*)\big(\rho_{33}^{*(0)}-\rho_{11}^{*(0)}\big)+\Omega_c\rho_{41}^{(0)}(|\Omega_p|^2-|\Omega_c|^2+d_{21}^*d_{31}^*)}{a_1^*d_{31}^*+a_2^*|\Omega_p|^2-a_3^*|\Omega_c|^2}\Omega_s\\&+\frac{\Omega_p\rho_{32}^{(0)}(|\Omega_c|^2-|\Omega_p|^2-d_{43}d_{31}^*)}{a_1^*d_{31}^*+a_2^*|\Omega_p|^2-a_3^*|\Omega_c|^2}\Omega_s\equiv a_{42}^{(1)}\Omega_s,\end{aligned} \tag{B2c}$$

$$\begin{aligned}\rho_{43}^{(1)}=&\frac{\Omega_p(|\Omega_c|^2-|\Omega_p|^2-d_{21}^*d_{42})\big(\rho_{33}^{*(0)}-\rho_{11}^{*(0)}\big)+\rho_{41}^{(0)}(d_{21}^*d_{31}^*d_{42}-|\Omega_c|^2d_{42}+|\Omega_p|^2d_{31}^*)}{a_1^*d_{31}^*+a_2^*|\Omega_p|^2-a_3^*|\Omega_c|^2}\Omega_s\\&+\frac{\Omega_p\Omega_c^*\rho_{32}^{(0)}(d_{42}-d_{31}^*)}{a_1^*d_{31}^*+a_2^*|\Omega_p|^2-a_3^*|\Omega_c|^2}\Omega_s\equiv a_{43}^{(1)}\Omega_s,\end{aligned} \tag{B2d}$$

with other $\rho_{jl}^{(1)}$ being zero, and

$$a_1=d_{21}d_{42}^*d_{43}^*-d_{21}|\Omega_c|^2+d_{43}^*|\Omega_p|^2, \tag{B3a}$$

$$a_2=|\Omega_p|^2-|\Omega_c|^2+d_{21}d_{42}^*, \tag{B3b}$$

$$a_3=d_{42}^*d_{43}^*+|\Omega_p|^2-|\Omega_c|^2. \tag{B3c}$$

The second-order solution reads

$$\rho_{11}^{(2)} = \left\{ \frac{2\Gamma_{42}X_{32}|\Omega_c|^2 + X_{32}|\Omega_c|^2\Gamma_{31} + i\Gamma_3\Gamma_{42}}{X_{32}|\Omega_c|^2\Gamma_{31}(i\Gamma_4 + X_{41}|\Omega_p|^2)} \times \left(\frac{\Omega_p a_{43}^{*(1)}}{d_{41}^*} - \frac{\Omega_p^* a_{43}^{(1)}}{d_{41}} \right) + \left(\frac{\Gamma_{32}}{\Gamma_{31}X_{32}|\Omega_c|^2} - \frac{2i}{\Gamma_{31}} \right) \times \left(a_{31}^{*(1)} - a_{31}^{(1)} \right) \right\} \rho_{11}^{(0)} + \frac{1}{X_{32}|\Omega_c|^2} \left(\frac{\Omega_c a_{21}^{(1)}}{d_{32}^*} - \frac{\Omega_c^* a_{21}^{*(1)}}{d_{32}} \right) \rho_{11}^{(0)}|\Omega_s|^2, \tag{B4a}$$

$$\rho_{22}^{(2)} = \frac{(i\Gamma_3 + X_{32}|\Omega_c|^2)\Gamma_{42}X_{41}|\Omega_p|^2}{X_{32}|\Omega_c|^2\Gamma_{31}(i\Gamma_4 + X_{41}|\Omega_p|^2)} \rho_{11}^{(2)} - \frac{i\left(a_{31}^{(1)} - a_{31}^{*(1)}\right)(i\Gamma_3 + X_{32}|\Omega_c|^2)}{\Gamma_{31}X_{32}|\Omega_c|^2}|\Omega_s|^2 + \frac{\Gamma_{42}(i\Gamma_3 + X_{32}|\Omega_c|^2)}{X_{32}|\Omega_c|^2\Gamma_{31}(i\Gamma_4 + X_{41}|\Omega_p|^2)} \times \left(\frac{\Omega_p^* a_{43}^{(1)}}{d_{41}} - \frac{\Omega_p a_{43}^{*(1)}}{d_{41}^*} \right)|\Omega_s|^2 + \frac{1}{X_{32}|\Omega_c|^2} \times \left(\frac{\Omega_c^* a_{21}^{*(1)}}{d_{32}} - \frac{\Omega_c a_{21}^{(1)}}{d_{32}^*} + a_{31}^{*(1)} - a_{31}^{(1)} \right)|\Omega_s|^2, \tag{B4b}$$

$$\rho_{33}^{(2)} = \frac{\Gamma_{42}X_{41}|\Omega_p|^2}{\Gamma_{31}(i\Gamma_4 + X_{41}|\Omega_p|^2)} \rho_{11}^{(2)} + \frac{\Gamma_{42}}{\Gamma_{31}(i\Gamma_4 + X_{41}|\Omega_p|^2)} \times \left(\frac{\Omega_p^* a_{43}^{(1)}}{d_{41}} - \frac{\Omega_p a_{43}^{*(1)}}{d_{41}^*} \right)|\Omega_s|^2 - \frac{i\left(a_{31}^{(1)} - a_{31}^{*(1)}\right)}{\Gamma_{31}}|\Omega_s|^2, \tag{B4c}$$

$$\rho_{44}^{(2)} = \frac{X_{41}|\Omega_p|^2}{i\Gamma_4 + X_{41}|\Omega_p|^2} \rho_{11}^{(2)} + \frac{1}{i\Gamma_4 + X_{41}|\Omega_p|^2} \times \left(\frac{\Omega_p^* a_{43}^{(1)}}{d_{41}} - \frac{\Omega_p a_{43}^{*(1)}}{d_{41}^*} \right)|\Omega_s|^2, \tag{B4d}$$

$$\rho_{32}^{(2)} = \frac{\left[\left(\rho_{33}^{(2)} - \rho_{22}^{(2)} \right)\Omega_c - \Omega_s \rho_{21}^{*(1)} \right]}{d_{32}}, \tag{B4e}$$

$$\rho_{41}^{(2)} = \frac{\left[\left(\rho_{44}^{(2)} - \rho_{11}^{(2)} \right)\Omega_p - \Omega_s \rho_{43}^{(1)} \right]}{d_{41}}. \tag{B4f}$$

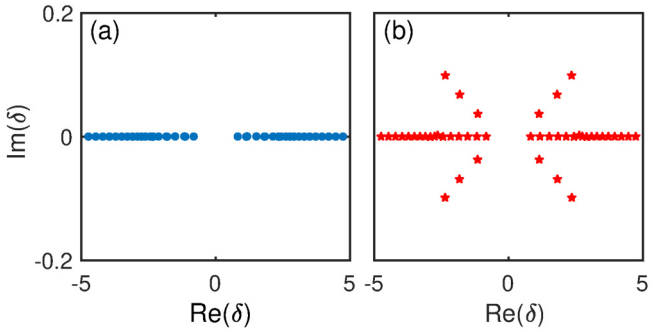

FIG. 10. Spectrum of the linear stability of the optical soliton as functions of Re(δ) and Im(δ), with δ the eigenvalue of the perturbations. (a) Linear stability spectrum of the soliton described in Fig. 5(a) (blue solid circles). (b) Linear stability spectrum of the soliton described in Fig. 5(b) (red stars).

The third-order solution for $\rho_{31}^{(3)}$ is given by

$$\rho_{31}^{(3)} = \frac{a_1\left(\rho_{33}^{(2)} - \rho_{11}^{(2)}\right) + a_2\Omega_p\rho_{41}^{*(2)} - a_3\Omega_c\rho_{32}^{*(2)}}{a_1 d_{31} + a_2|\Omega_p|^2 - a_3|\Omega_c|^2}|\Omega_s|^2\Omega_s \equiv a_{31}^{(3)}|\Omega_s|^2\Omega_s. \tag{B5}$$

The other density-matrix elements in this order are not needed and hence omitted here.

APPENDIX C: LINEAR STABILITY ANALYSIS OF SOLITONS

The linear stability analysis [46,47] on the solitons shown in Figs. 5(a) and 5(b) is implemented by assuming $u = [u_0(\xi) + f(\xi)\exp(i\delta\zeta) + g^*(\xi)\exp(-i\delta^*\zeta)]\exp(iq\zeta)$. Here $u_0(\xi)\exp(iq\zeta)$ is the soliton wave function, $f(\xi)\exp(i\delta\zeta)$ and $g^*(\xi)\exp(-i\delta^*\zeta)$ are perturbations, and δ is the eigenvalue of the perturbations. Substituting this expression into Eq. (4), we obtain the linear eigenvalue problem for the perturbations:

$$\begin{bmatrix} \mathcal{L}_{11} & Wu_0^2 \\ -(Wu_0^2)^* & \mathcal{L}_{22} \end{bmatrix} \begin{bmatrix} f \\ g \end{bmatrix} = \delta \begin{bmatrix} f \\ g \end{bmatrix}, \tag{C1}$$

with $\mathcal{L}_{11} = \partial_{\xi\xi} - V(\xi) - 2W(\xi)|u_0|^2 - q$ and $\mathcal{L}_{22} = -\partial_{\xi\xi} + V^*(\xi) + 2W^*(\xi)|u_0|^2 + q$. Equation (C1) can be solved numerically by the using plane-wave expansion method [50,51]. The eigenspectrum of Eq. (C1) for the soliton is shown in Fig. 10. The soliton described in Fig. 5(a) is stable because Im(δ) = 0 [see Fig. 10(a)]; however, the soliton described in Fig. 5(b) is unstable because some Im(δ) are negative [see Fig. 10(b)].

[1] S. Boettcher and C. M. Bender, Real Spectra in Non-Hermitian Hamiltonians Having $\mathcal{PT}$ Symmetry, Phys. Rev. Lett. **80**, 5243 (1998).

[2] C. M. Bender, Making sense of non-Hermitian Hamiltonians, Rep. Prog. Phys. **70**, 947 (2007).

[3] R. El-Ganainy, K. G. Makris, M. Khajavikhan, Z. H. Musslimani, S. Rotter, and D. N. Christodoulides, Non-Hermitian physics and $\mathcal{PT}$ symmetry, Nat. Phys. **14**, 11 (2018).

[4] L. Feng, R. El-Ganainy, and L. Ge, Non-Hermitian photonics based on parity-time symmetry, Nat. Photon. **11**, 752 (2017).

[5] H. Zhao and L. Feng, Parity-time symmetric photonics, Rev. Sci. Nat. **5**, 183 (2018).

[6] Z. Lin, H. Ramezani, T. Eichelkraut, T. Kottos, H. Cao, and D. Christodoulides, Unidirectional Invisibility Induced by $\mathcal{PT}$-Symmetric Periodic Structures, Phys. Rev. Lett. **106**, 213901 (2011).

[7] L. Feng, Y.-L. Xu, W. S. Fegadolli, M.-H. Lu, J. E. B. Oliveira, V. R. Almeida, Y.-F. Chen, and A. Scherer, Experimental demonstration of a unidirectional reflectionless parity-time metamaterial at optical frequencies, Nat. Mat. **12**, 108 (2012).

[8] C. Bender, S. Factor, J. D. Bodyfelt, H. Ramezani, D. N. Christodoulides, F. M. Ellis, and T. Kottos, Observation of Asymmetric Transport in Structures with Active Nonlinearities, Phys. Rev. Lett. **110**, 234101 (2013).

[9] B. Peng, S. K. Özdemir, F. Lei, F. Monifi, M. Gianfreda, G. L. Long, S. Fan, F. Nori, C. M. Bender, and L. Yang, Parity-time-symmetric whispering-gallery microcavities, Nat. Phy. **10**, 394 (2014).

[10] L. Chang, X. Jiang, S. Hua, C. Yang, J. Wen, L. Jiang, G. Li, G. Wang, and M. Xiao, Parity-time symmetry and variable optical isolation in active-passive-coupled microresonators, Nat. Photonics **8**, 524 (2014).

[11] S. Longhi, $\mathcal{PT}$-symmetric laser absorber, Phys. Rev. A **82**, 031801(R) (2010).

[12] Y. D. Chong, L. Ge, and A. D. Stone, $\mathcal{PT}$-Symmetry Breaking and Laser-Absorber Modes in Optical Scattering Systems, Phys. Rev. Lett. **106**, 093902 (2011).

[13] Y. Sun, W. Tan, H. Li, J. Li, and H. Chen, Experimental Demonstration of a Coherent Perfect Absorber with $\mathcal{PT}$ Phase Transition, Phys. Rev. Lett. **112**, 143903 (2014).

[14] V. V. Konotop, V. S. Shchesnovich, and D. A. Zezyulin, Giant amplification of modes in parity-time symmetric waveguides, Phys. Lett. A **376**, 2750 (2012).

[15] L. Feng, Z. J. Wong, R. Ma, Y. Wang, and X. Zhang, Single mode laser by parity-time symmetry breaking, Science **346**, 972 (2014).

[16] H. Hodaei, M.-A. Miri, M. Heinrich, D. N. Christodoulides, and M. Khajavikhan, Parity-time-symmetric microring lasers, Science **346**, 975 (2014).

[17] H. Hodaei, A. U. Hassan, S. Wittek, H. Garcia-Gracia, R. El-Ganainy, D. N. Christodoulides, and M. Khajavikhan, Enhanced sensitivity at higher-order exceptional points, Nature (London) **548**, 187 (2017).

[18] W. Chen, Ş. K. Özdemir, G. Zhao, J. Wiersig, and L. Yang, Exceptional points enhance sensing in an optical microcavity, Nature (London) **548**, 192 (2017).

[19] L. Xiao, X. Zhan, Z. H. Bian, K. K. Wang, X. Zhang, X. P. Wang, J. Li, K. Mochizuki, D. Kim, N. Kawakami, W. Yi, H. Obuse, B. C. Sanders, and P. Xue, Observation of topological edge states in parity-time-symmetric quantum walks, Nat. Phys. **13**, 1117 (2017).

[20] S. V. Suchkov, A. A. Sukhorukov, J. Huang, S. V. Dmitriev, C. Lee, and Y. S. Kivshar, Nonlinear switching and solitons in $\mathcal{PT}$-symmetric photonic systems, Laser Photon. **10**, 177 (2016).

[21] V. V. Konotop, J. Yang, and D. A. Zezyulin, Nonlinear waves in $\mathcal{PT}$-symmetric system, Rev. Mod. Phys. **88**, 035002 (2016).

[22] C. Hang, G. Huang, and V. V. Konotop, $\mathcal{PT}$ Symmetry with a System of Three-Level Atoms, Phys. Rev. Lett. **110**, 083604 (2013).

[23] J. Sheng, M.-A. Miri, D. N. Christodulides, and M. Xiao, $\mathcal{PT}$-symmetric optical potentials in a coherent atomic medium, Phys. Rev. A **88**, 041803(R) (2013).

[24] Z. Zhang, Y. Zhang, J. Sheng, L. Yang, M.-A. Miri, D. N. Christodoulides, B. He, Y. Zhang, and M. Xiao, Observation of Parity-Time Symmetry in Optically Induced Atomic Lattices, Phys. Rev. Lett. **117**, 123601 (2016).

[25] C. Hang and G. Huang, Parity-time symmetry with coherent atomic gases, Adv. Phys.: X **2**, 737 (2017).

[26] Z. Zhang, D. Ma, J. Sheng, Y. Zhang, and M. Xiao, Non-Hermitian optics in atomic systems, J. Phys. B: At., Mol., Opt. Phys. **51**, 072001 (2018).

[27] C. Hang and G. Huang, Weak-light solitons and their active control in a parity-time-symmetric atomic system, Phys. Rev. A **91**, 043833 (2015).

[28] C. Hang and G. Huang, Parity-time symmetry along with nonlocal optical solitons and their active controls in a Rydberg atomic gas, Phys. Rev. A **98**, 043840 (2018).

[29] F. Kh. Abdullaev, V. V. Konotop, M. Salerno, and A. V. Yulin, Dissipative periodic waves, solitons, and breathers of the nonlinear Schrödinger equation with complex potentials, Phys. Rev. E **82**, 056606 (2010).

[30] F. K. Abdullaev, Y. V. Kartashov, V. V. Konotop, and D. A. Zezyulin, Solitons in $\mathcal{PT}$-symmetric nonlinear lattices, Phys. Rev. A **83**, 041805(R) (2011).

[31] D. A. Zezyulin, Y. V. Kartashov, and V. V. Konotop, Stability of solitons in $\mathcal{PT}$-symmetric nonlinear potentials, Europhys. Lett. **96**, 64003 (2011).

[32] Y. He, X. Zhu, D. Mihalache, J. Liu, and Z. Chen, Lattice solitons in $\mathcal{PT}$-symmetric mixed linear-nonlinear optical lattices, Phys. Rev. A **85**, 013831 (2012).

[33] C. Huang, C. Li, and L. Dong, Stabilization of multipole-mode solitons in mixed linear-nonlinear lattices with a $\mathcal{PT}$ symmetry, Opt. Express **21**, 3917 (2013).

[34] Y. Meng and Y. Liu, Power-dependent shaping of solitons in parity time symmetric potentials with spatially modulated nonlinearity, J. Opt. Soc. Am. B **30**, 1148 (2013).

[35] J. Xie, W. Chen, J. Lv, Z. Su, C. Yin, and Y. He, Nonlocal defect solitons in parity-time-symmetric photonic lattices with spatially modulated nonlinearity, J. Opt. Soc. Am. B **30**, 1216 (2013).

[36] X. Zhu, Z. Shi, and H. Li, Gap solitons in parity-time-symmetric mixed linear-nonlinear optical lattices with fourth-order diffraction, Opt. Commun. **382**, 455 (2017).

[37] M. Nazari, F. Nazari, and M. K. Moravvej-Farshi, Dynamic behavior of spatial solitons propagating along Scarf II parity-time symmetric cells, J. Opt. Soc. Am. B **29**, 3057 (2012).

[38] F. Kh. Abdullaev, V. A. Brazhnyi, and M. Salerno, Scattering of gap solitons by $\mathcal{PT}$-symmetric defects, Phys. Rev. A **88**, 043829 (2013).

[39] U. Al Khawaja, S. M. Al-Maraoug, H. Bahlouli, and Yuri S. Kivshar, Undirectional soliton flows in $\mathcal{PT}$-symmetric potentials, Phys. Rev. A **88**, 023830 (2013).

[40] S. M. Al-Marzoug, Scattering of solitons by complex $\mathcal{PT}$ symmetric Gaussian potentials, Opt. Express **22**, 22080 (2014).

[41] N. Karjanto, W. Hanif, B. A. Malomed, and H. Susanto, Interactions of bright and dark solitons with localized-symmetric potentials, Chaos **25**, 023112 (2015).

[42] H. Kang, L. Wen, and Y. Zhu, Normal or anomalous dispersion and gain in a resonant coherent medium, Phys. Rev. A **68**, 063806 (2003).

[43] We see moreover that amplitudes of the linear and nonlinear susceptibilities (both their real and imaginary parts) are enhanced when the control field is increased, which is due to the EIT effect of the system.

[44] Other types of space-dependent control field, e.g., a periodic laser intensity distribution in space, can also be adopted to realize the combined periodic linear-nonlinear optical potentials with $\mathcal{PT}$ symmetry, which are not considered here.

[45] J. Yang, *Nonlinear Waves in Integrable and Nonintegrable System* (SIAM, Philadelphia, 2010).

[46] S. Nixon, L. Ge, and J. Yang, Stability analysis for solitons in $\mathcal{PT}$-symmetric optical lattices, Phys. Rev. A **85**, 023822 (2012).

[47] L. Ge, M. Shen, T. Zang, C. Ma, and L. Dai, Stability of optical solitons in parity-time-symmetric optical lattices with competing cubic and quintic nonlinearities, Phys. Rev. E **91**, 023203 (2015).

[48] The relation between the incident velocity v and the incident angle θ of the soliton is $\theta = \tan^{-1}(2v)$.

[49] R. W. Boyd, *Nonlinear Optics*, 3rd ed. (Academic, New York, 2008).

[50] P. Griffin, P. Nagel, and R. D. Koshel, The plane wave expansion method, J. Math. Phys. **15**, 1913 (1974).

[51] K. G. Makris, Z. H. Musslimani, D. N. Christodoulides, and S. Rotter, Constant-intensity waves and their modulational instability in non-Hermitian potentials, Nat. Commun. **6**, 7257 (2015).